Using Deep Learning to Map Quaternary Faults in Western USA

Bastien HERMANT, Lauriane KIERSNOWSKI, Mathieu BELLANGER

91 Chemin de Gabardie, 31500, Toulouse, FRANCE

bastien.hermant@tls-geothermics.com

Keywords: Deep learning, fault mapping, Quaternary faults

1. ABSTRACT

Faults are an essential component of geothermal systems, particularly in the Great Basin region where most hydrothermal systems are fault-controlled. Accurate and complete fault mapping is therefore of prime importance for assessing the geothermal favorability of an area or a prospect, as it allows for defining the structural network, its orientation with respect to the stress field and the potential favorable structural settings (step-over, accommodation zone, etc). Quaternary faults databases exist across the western USA. However, their accuracy and the homogeneity of mapping between the sub-regions/states is sometimes insufficient for an objective analysis of favorability at a regional scale. This could create a bias between regions where fault mapping is robust and those where it is incomplete. To overcome this bias, TLS Geothermics has developed a deep learning approach using convolution neural networks for geological fault detection based on remote sensing images. By selecting the appropriate data, the neural network can produce fault prediction maps at regional scale. It can therefore be used to better assess geothermal potential at a regional scale. Using an adapted version of the neural network on a local scale and with higher resolution remote sensing data can also provide more robust structural models on a prospect scale.
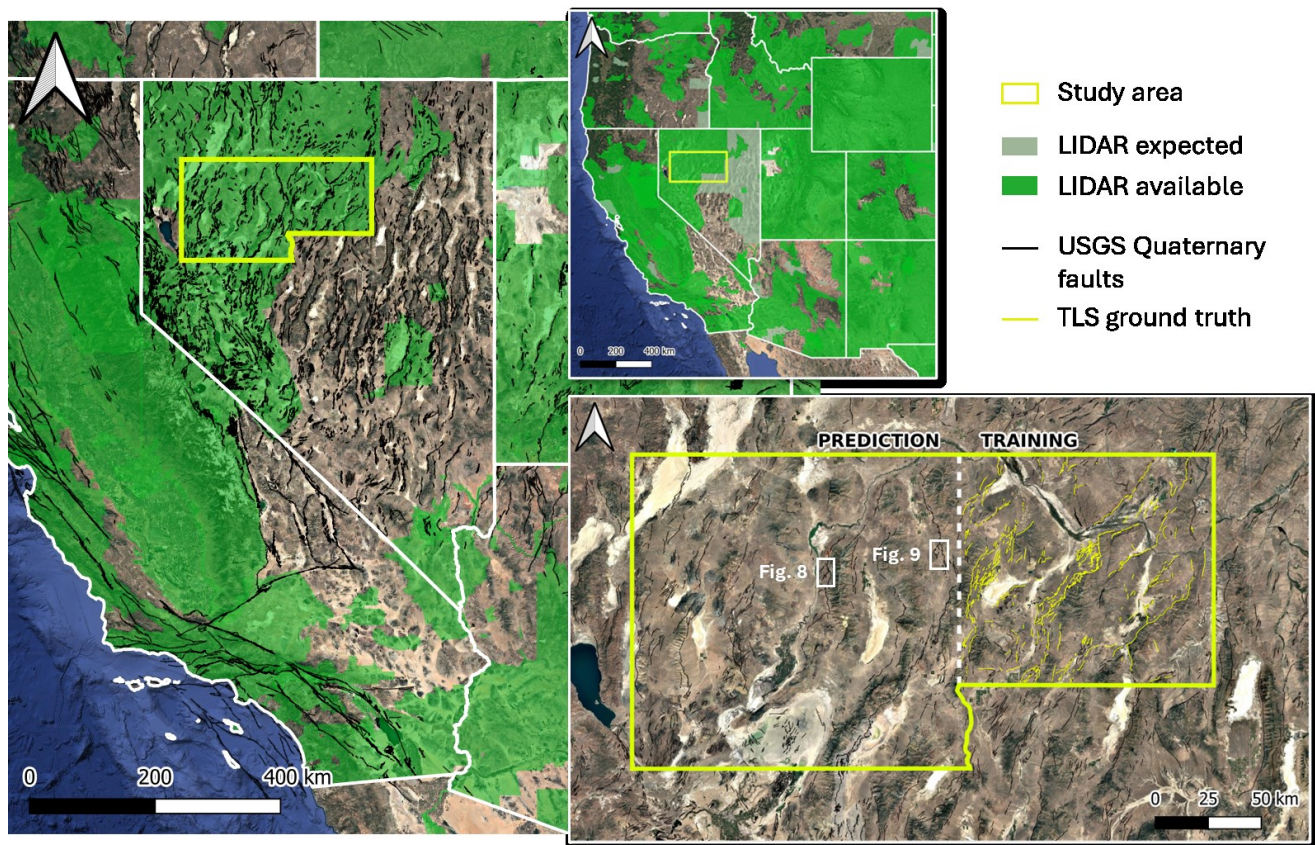
2. INTRODUCTION

Figure 1: Map of the study area in the northern central Nevada showing the LIDAR data coverage and the extent of the training area with the associated fault label. USGS Quaternary faults are also shown as black lines. Location of zoom area in Figure 8 and Figure 9 are shown on the prediction area as white rectangles.

Faults and fractures are widespread in the Earth's crust. They are a key parameter for many geosciences topics including resource exploration (hydrocarbons, minerals, geothermal) and geological hazards (earthquakes, induced seismicity or landslides). Faults can span a wide range of length scales (10^{-6} - 10^3 km) and surface to depth widths ($1 - 100$ km) and have a complex 3D and internal architecture

(Caine et al., 1996; Curewitz and Karson, 1997; Wesnousky, 1988). At all scales, the fault network is composed of major faults of potentially complex geometry and a set of secondary fractures and faults (the damage zone) that more or less intensely dissect the host rock around the main fault, sometimes to great distances from it (Chester and Logan, 1986; Faulkner et al., 2011; Mitchell and Faulkner, 2009).

This fault network is of prime importance for geothermal systems because it has a strong influence on the permeability (Bense et al., 2013; Caine et al., 1996; Evans et al., 1997). Indeed, most of the geothermal systems in the Western North America have fault-controlled permeability (Barton et al., 1997; Faulds et al., 2010; Jolie et al., 2015). However, faults can also act as barriers to fluid flow and compartmentalize geothermal systems (Caine et al., 1996; Kaven et al., 2011). The behavior of fault permeability depends on several parameters including: the deformed lithologies (Bense et al., 2013), the density and aperture of the fractures and faults (Baghbanan and Jing, 2008; J. E. Gale, 1982; Gao et al., 2020), potential scaling and alteration (Bense et al., 2013; Detwiler and Morris, 2018) and the orientation of the faults relative to the local stress field (Baghbanan and Jing, 2008; Barton et al., 1995; Detwiler and Morris, 2018; John E. Gale, 1982). The geometry of the major fault segments can thus have an influence on these parameters and forms specific structural settings (Curewitz and Karson, 1997; Faulds and Hinz, 2015), which imply fracture network complexity and a variation in the local stress and strain fields that favour permeability and fluid circulation (Siler, 2023; Siler et al., 2018, 2016). Therefore, accurate and reliable fault mapping is essential at all stages of geothermal system exploration. It is even more important in the prospecting and early exploration phases, when no geophysical or drilling data are available.

Western North America contains a diffuse plate boundary, characterized by dextral motion between the Pacific and North American plates (Atwater and Stock, 1998) and west-northwest-directed extension within the Basin and Range Province (Jones et al., 1992). The San Andreas fault system accommodates ~80% of the plate motion while the remaining ~20% is accommodated by the right-lateral strike-slip fault system of the Walker Lane (Faulds et al., 2005; Hammond and Thatcher, 2007; Kreemer et al., 2009). A broad zone of active WNW-directed extension stretches eastward across the Great Basin region to absorb north-westward declining dextral motion in the Walker Lane. Given this tectonic activity, Western North America and especially the Basin and Range Province in extensive motion, are particularly well suited to mapping surface faults. Many faults induce local topographic variations (fault scarp) that can be mapped from elevation, slope or satellite imagery data (Johnson et al., 2014; MacKnight et al., 2004).
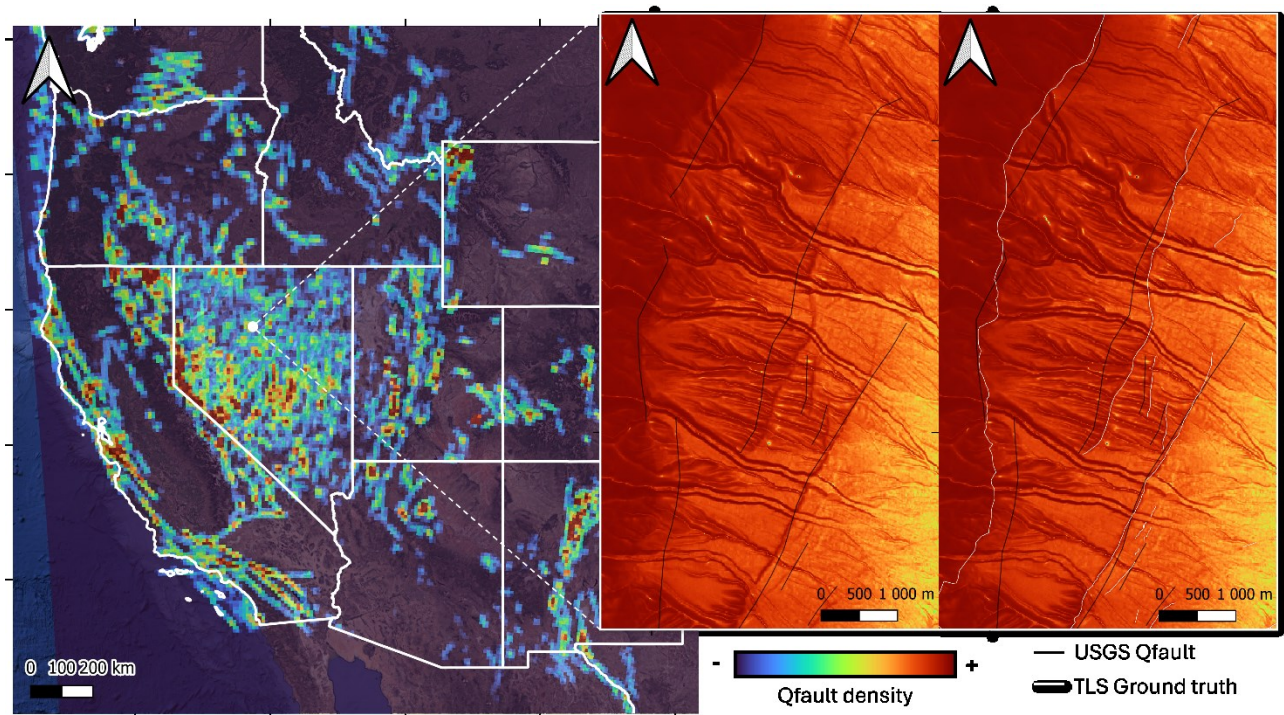

Figure 2: (Left) USGS Quaternary fault density map highlighting the regional variation in Quaternary fault mapping that is not only due to the geological context: northern Nevada compared to southern Idaho and Oregon, some local high density in Arizona compared to state scale mapping; (Right) Local discrepancy observed in North Central Nevada: distance between USGS Quaternary faults and TLS fault label can be up to 400m.

Databases of these most recent faults exist, especially the USGS Quaternary Fault Database. However, the mapping is occasionally imprecise at small scale or of variable and heterogeneous accuracy at large scale (Figure 1). The local imprecision may be due to the resolution of the available data for mapping at the time the database was created. The heterogeneity of fault mapping may be due to the aggregation of different mapping sources or scales in this database. Indeed, some areas where the geology has been mapped more precisely have an artificially higher fault density and accuracy than areas where geological and structural mapping has been done at a larger scale. Improvements in the available digital elevation models and satellite imagery (coverage and resolution) now make it possible to map

2

Quaternary faults more accurately and consistently. However, this work is very time consuming when carried out by a human operator and can lead to biased mapping.

To address this challenge, we propose to harness the power of artificial intelligence (AI) and, in particular, convolutional neural networks (CNN) (LeCun et al., 2015). CNN has revolutionized numerous applications in computer vision, natural language processing, and behavioral analysis (Sturman et al., 2020; Vouloudimos et al., 2018). Among the various algorithms, CNNs have shown great potential for tackling the complex task of image data analysis and the ability to rapidly process large amounts of data (Krizhevsky et al., 2012; Russakovsky et al., 2015; Simonyan and Zisserman, 2015). In the geosciences, the CNNs have already shown powerful results for feature detection on images or in 3D physical models with applications including seismic inversion (Das et al., 2019) or interpretation (Waldeland et al., 2018; Wrona et al., 2021; Xiong et al., 2018) and feature detection on remote images (Ding et al., 2016; Mattéo et al., 2021; Palafox et al., 2017). In our study, CNNs are trained with image data (composed of elevation, slope and satellite data) and labels ("ground truth" faults mapped by a human operator on a small-scale area where the Quaternary fault signature is clear). As a small number of training data could lead to low performance, a data augmentation step is performed to greatly increase the number of training data. The training hyperparameters are currently chosen arbitrarily, but are being optimized in a dedicated work to obtain the best prediction performance on a set of test images (not used for training). The trained model is then able to predict faults over a much larger area, allowing exploration geologists to map the complexity of the fault network more accurately.
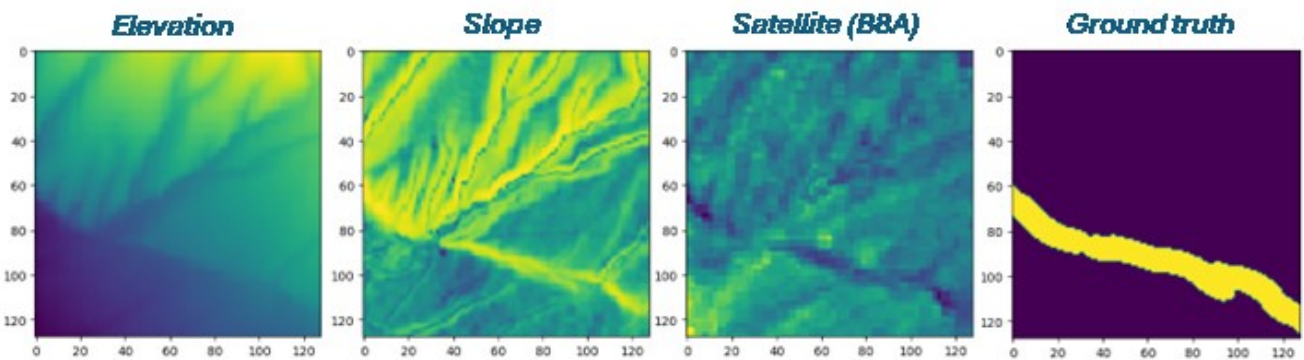
3. DATA AND LABELS

Figure 3: Example of a data image (128 x 128 x 3) including elevation, slope and Sentinel-2 B8A bands, and the associated fault label mapped by human operators.

3.1. Digital Elevation Model (DEM)

The elevation maps are provided through the 3D Elevation Program (3DEP), an initiative led by the USGS to collect and make available high-quality elevation data for the whole US territory (USGS 3D Elevation Program). The elevation dataset is derived from various source datasets that are processed to a specification with a consistent resolution, coordinate system, elevation units, and horizontal and vertical datums. For this study, we chose to use the 1/3 arc-second elevation data, at raster format, because it is the highest resolution seamless DEM dataset for the US with full coverage of the 48 conterminous states, Alaska, Hawaii, and US territories. The ground spacing is approximately 10 m North/South, but varies East/West due to meridian convergence with latitude. This resolution was also chosen because (1) it allows an operator to see most of the fault scarps to define the fault labels and qualitatively assess prediction performance, (2) it requires less computational space than a 1 m-resolution DEM.

The slope raster, representing the inclination of a surface, is calculated from the elevation data. However, the quality of the slope calculation is significantly degraded by strong artefacts in some specific areas. After analysis, these areas correspond to areas where no LIDAR (Laser Imaging Detection And Ranging) data are available. This means that clean slope raster data can only be calculated where elevation data is derived from LIDAR data. Therefore, we chose to use the 1/3 arc-second elevation data, but only where it is derived from LIDAR data, in the northern central Nevada (USGS 3D Elevation Program).

3.2. Satellite imagery

To add independent data from elevation and slope, satellite images are also considered for training deep learning neural network. Among the available satellite imagery, the choice has been made to use images from Sentinel-2, an Earth observation mission launched by the European Space Agency (ESA) as part of the Copernicus program (https://www.copernicus.eu/fr). The mission comprises a constellation of satellites, with the two first (Sentinel-2A and Sentinel-2B) launched in 2015 and 2017 respectively. Sentinel-2 satellites acquire data over 13 spectral bands—four bands (blue, green, red, near infra-red—NIR) at 10 m resolution and six other bands (including shortwave infra-red—SWIR) at 20 m resolution. Therefore, these resolutions are consistent with the 10 m-resolution of elevation and slope data.

The satellite has a repetition frequency, i.e. the frequency at which the satellite passes over the same over the same area, 5 to 10 days depending on the area. Due to the large size of the dataset, Sentinel-2 products are distributed as tiles of 1 x 1 degree. In addition, the satellite images selected must be as clean as possible, avoiding artefacts like clouds, smoke from wildfire, shadows from the sun's angle

on topography, and snow. Therefore, we have used Sentinel-2 data processed at level 2A by CNES images from Sentinel-A and we have carefully selected tiles from those available in the early afternoon, during summer to fall, and without clouds.

Among the available spectral bands, we chose only the B8A band to avoid making the training images too heavy and to keep the study within the available computing capacity. The B8A band, with a resolution of 20 m down-sampled to 10 m, is a visible and near-infrared centered in 865 nm wavelength with a bandwidth of 20 nm. It was chosen after testing all the bands and an analysis of the spectral signature of the fault pixel across all the spectral bands of Sentinel-2 which are not detailed in this publication. Note that the B8A band is likely to be suitable due to its ability to detect biomass content and to analyse or classify vegetation. This may be important in some areas of very flat topography where faults are not necessarily highlighted by elevation data but sometimes by vegetation orientation.

3.3. Fault label derived from manual mapping

The fault label is used to check that the model predictions are accurate and to adjust the model parameters accordingly. The characteristics of a fault label for training an algorithm include its quality (the accuracy of the labels assigned to the data), quantity (the size of the dataset, which must be large enough to avoid overlearning and ensure correct generalization) and representativeness (the variety of the data, which must cover all possible cases that the model could encounter in its actual use). The use of a high-quality fault label, in sufficient quantity and representativeness, is essential for training an accurate and efficient neural network.

As the USGS Quaternary fault mapping is sometimes inaccurate at small scales or of variable precision, we created a new manual mapping of faults over the eastern half of the study area using elevation and slope data, and satellite imagery. The remaining half was reserved for prediction (Figure 1; Figure 2). The main visual characteristics of the fault object that help to identify it are:

- ✓ A fault often appears as a generally straight line on the image, creating a strong visual contrast with the surrounding areas
- ✓ Active or recent faults can affect the topography: the areas on either side of the fault will have a different elevation and the fault zone itself will have a steeper slope.
- ✓ Faults can affect the surrounding vegetation, creating a noticeable variation in vegetation on different parts of the Earth's surface.
- ✓ Geological features can also be associated with the presence of faults in the area, such as areas of weathered rock or fractures along hillsides or mountains.

Using these criteria, we created a fault label dataset containing 1100 faults with a cumulative length of 264 km. These faults, initially in shapefile format, are converted to a binary raster, with pixels crossed by a fault taking the value 1. As the expression of a fault on the data can be thicker than the resolution of the data used (10 m), a buffer is applied around the fault pixels: all pixels in this buffer take the value 1. As the effect of this buffer on the quality of the prediction is unknown at this stage, but could help in the learning phase, a buffer value of 50 m was used, implying a thickness of the fault signature in the data 100 m. The raster created are used to generate the label images in the dataset creation phase.

4. DEEP LEARNING METHODOLOGY

4.1. Principles of deep learning and Convolutional Neural Networks (CNN)

A neuron is an input function f_j with $x = (x_1, \ldots, x_d)$, weighted by a vector of weights $w_j = (w_{\{j,1\}}, \ldots, w_{\{j,d\}})$, completed by the bias b_j and associated with an activation function φ with $f_j(x) = \varphi(w_j, x > +b_j) = \varphi(a_j(x))$. There are various activation functions including identity, sigmoid, hyperbolic tangent, threshold, Rectified Linear Unit (ReLU). Artificial Neural Networks (ANNs) consist of a connected set of neurons, each of which is trained to generate a specific decision boundary and classify simple spaces. The weights of each neuron are incrementally adjusted by the network to optimize a predefined cost (or loss) function. The layers within an ANN can be of different types and these different layers are connected in a sequential order so that the input of one layer is the output of the previous one (Figure 4). Traditionally, ANNs have an input layer that receives the input data; a set of hidden layers, which serve as the classifier; and an output layer that provides the result of the classification (Hornik et al., 1989).

CNNs differ from the ordinary ANNs in that different inputs share weights, rather than each input having a single weight (LeCun et al., 1995, 1989). CNNs extract features in the image matrix using convolutions that help to extract the most descriptive features in an image. CNNs are typically composed of (1) convolutional layers, which perform a convolutional product between a filter (kernel) to learn the convolutions that best represent the classes in the data; (2) pooling layers which use a filter that scans the input matrix and retains only the maximum value, allowing the number of features from the convolutions to be reduced, thereby improving computational performance (Nair and Hinton, 2010), controlling overfitting and allowing for translation invariance; (3) ReLU layers, which apply the ReLU activation function (Nair and Hinton, 2010) to enhance the non-linear properties of the network. A typical CNN contains many layers with kernels that interact hierarchically to extract the relevant feature in an image. The "depth" of a CNN is related to the number of layers in the architecture of the CNN.

4.2. Architecture of the CNN models

The U-Net architecture (Ronneberger et al., 2015) includes two sub-networks, called the encoder and decoder, with skip connections between the encoder and decoder units (Figure 4). The encoder down-samples and coarse-grains the data through "pooling layers", which are typically added after each or a short series of convolutional layers. This pooling operation consists of a sliding window that scans the output of the previous layer, looking for the maximum ("max pooling") value at each position of the scan (Boureau et al., 2010). The pooling operations thus reduce the size of the feature maps, allowing the next filters to have a larger field of view of the data, and thus the

capacity to identify larger motifs. As the encoder down-samples the data, the searched features can be accurately detected but their localization is not accurately recovered. Therefore, a decoder subnetwork is added to up-scale the data and enables the localization of the identified features. To facilitate the encoding-decoding process, the model is designed to be symmetric, with the output of each block in the encoder being concatenated to the input of its symmetric counterpart in the decoder. Each block in the decoder performs the same number of convolution operations as its counterpart in the encoder, but these are followed by an upscaling operation. A final convolution layer with a sigmoid activation function produces the output image from the probability for each pixel to belongs to the feature class, a Quaternary fault in our study.
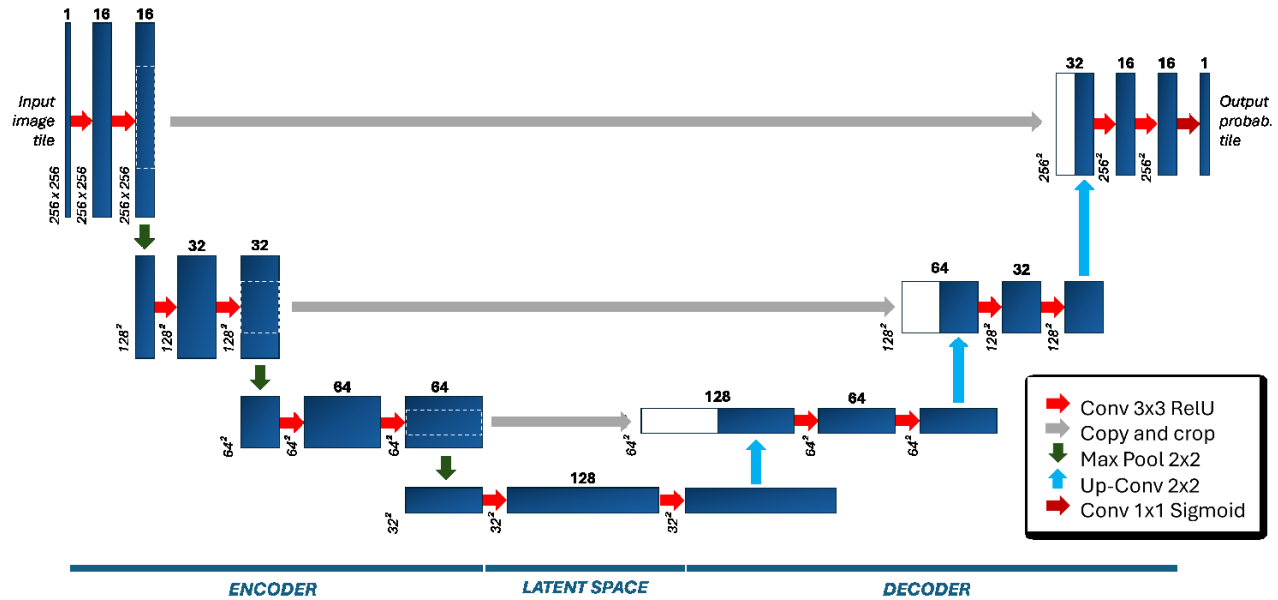

Figure 4: Simplified U-net (siUNET) architecture used for fault prediction considering 256 x 256 input image tiles and 256 x 256 probability image output. Each blue box corresponds to a multi-channel feature map. The number of channels is indicated at the top of the box. The x-y size is given at the bottom left of the box. White boxes represent copied feature maps. The arrows indicate the different operations (modified from Ronneberger et al., 2015).

In this study, we used two different CNN models based on a U-net architecture: a simplified version of U-Net model (called siUNET; Figure 4) and the FaultSEG model, developed by TLS Geothermics. The siUNET model (Figure 4) was designed to test the effectiveness of CNNs for predicting Quaternary faults from elevation and satellite data. With a total of 487297 parameters, it is relatively simple and can be easily trained for rapid application. The FaultSEG model was developed later to achieve the best possible performances for the same task as siUNET. It is a deeper CNN with more blocks in the encoder and decoder. The blocks themselves contain more convolutional layers and a larger number of channels. As a result, the number of parameters to be trained is about 100 times greater than with siUNET, and the learning and prediction times are therefore longer.

5. TRAINING PROCESS

5.1. Training, validation and test dataset creation process

Data creation

The learning, validation and test datasets are created using the following procedure:

- ✓ The multiband image (elevation, slope and satellite) of the study area is divided into tiles of the desired size. Given the resolution of the images used (10 m) and the size of the signature of the fault objects (10^2 - 10^5 m long and 10 - 10^2 m wide), an image size of 128 x 128 pixels, i.e. 1280 x 1280 m, was chosen. This size makes it possible to show all or part of a fault, or even several faults in the same image, while limiting the size of the images. An equivalent split is performed on the label image to obtain the label tile corresponding to each multiband data tile.
- ✓ Only tiles whose labels contain at least one fault pixel (value 1) are retained. This filtering step makes it possible to (1) limit the imbalance in the training data (very few fault pixels with a value of 1 compared with pixels with a value of 0) and (2) limit the possibility of learning images without mapped faults when there should be some due to operator observation bias. At this stage, 7692 tiles are retained for 50 m buffer.
- ✓ Randomly divide the retained tiles into a training set, a validation set and a test set with 64%, 16% and 20% proportion respectively. Therefore, at this stage, the training, validation and test datasets contains 4920, 1232 and 1540 images respectively.

5

Data normalization

Since each image tile has a different topography, slope and satellite image value, there is a need to normalize the training, validation and test data. Indeed, without this normalization step, the training from one image or batch of images is not transferable to different images. Therefore, each image is normalized and centered per band using the following equation:

$$X'_i = \frac{X_i - \mu_i}{\sigma_i}$$

Where i is the indices of the band, X' the normalized image, X the original image, μ the mean and σ the standard deviation

This image normalization process involves vertical exaggeration of the relief in relatively flat areas (sedimentary basin center, playa). This effect is intended because it helps to identify structures in these flat areas. However, it also means that features other than Quaternary faults may be exaggerated. Prediction results in flat areas should therefore be treated with caution.
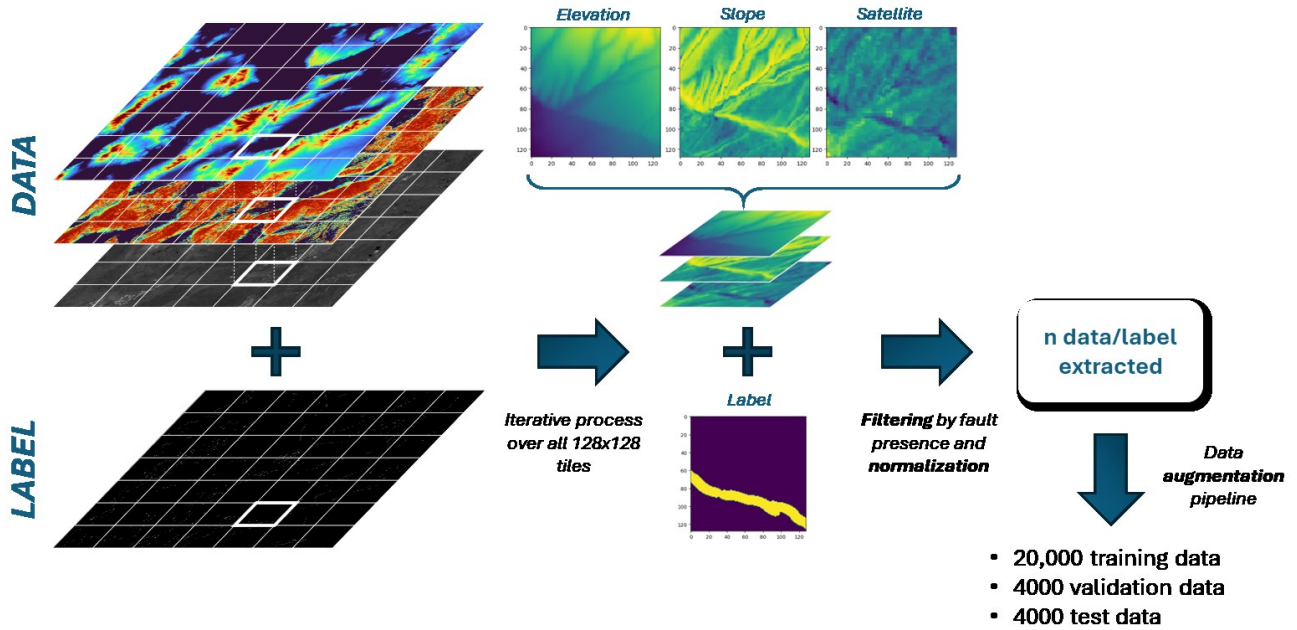

Figure 5: Data processing to produce efficient training, test and validation datasets from elevation, slope and satellite data, and fault labels.

Data augmentation

Data augmentation is essential to teach the network the desired invariance and robustness properties, when only few training samples are available (Ronneberger et al., 2015). In our study, there is a relatively small volume of fault label available (~ 7700 images) due to the time required for the manual fault picking, inducing a small number of training data. It may involve difficulties in training and potentially over-fitting, when the model learns so much from a specific dataset that it becomes unable to predict anything else than this dataset. Therefore, to prevent this bias and improve the training performances, we artificially augmented the dataset, using the *Albumentations* Python library (Buslaev et al., 2020), by applying pixel-level and spatial-level transformations including: random change of brightness and contrast, random change of hue and saturation values, random gamma correction, flip transformations, 90° rotations, transposition, grid distortion and elastic transform.

A specific pipeline of augmentation transformation is applied to the normalized dataset with probability function associated to each possible transformation. Then, a dataset containing 20000 images for training, 4000 images for validation and 4000 images for test is generated, inducing 72%, 14% and 14% proportion respectively. Note that the degree of overfitting is monitored during training by evaluating the model performance on the independent validation data set, which is not used to constrain the model parameters directly.

5.2. Loss function and metrics for estimating the performances of the model

The objective of our study and the data used involves a strong class imbalance in the data and in the expected predictions. Indeed, even with a buffer around the faults, the pixels classified 1 (fault) are much less numerous than the pixels classified 0 (non-fault): the proportion of fault pixels is 6.5%. Consequently, the loss function and the metrics chosen to evaluate model performance must take this behavior into account.

The class imbalance involves the non-fault class will dominate the classic binary cross entropy loss, causing the model to become more confident in predicting non-fault class while putting less emphasis on the fault class. Moreover, binary cross entropy loss fails to pay more

6

attention to hard examples, those in which the model repeatedly makes huge errors rather than those which are easily classified. To solve these problems, we used Focal Binary Cross Entropy loss (Lin et al., 2018):

$$FocalCrossEntropy = -\sum_{i=1}^{i=n} \alpha \cdot (1-p_i)^\gamma \cdot log(p_i)$$

Where p_i is the predicted probability of class 1, α the balancing factor and γ the focusing parameter.

Focal Binary Cross Entropy loss uses a "focal factor" $(1-p_i)^\gamma$ to down-weight easy examples and focus more on hard examples, ensuring that predictions on hard examples improve over time rather than becoming overly confident with easy ones. This loss function naturally solved the problem of class imbalance because examples from the majority class are usually easy to predict while those from the minority class are hard due to a lack of data or examples from the majority class dominating the loss and gradient process. In our study, α value is 0.065 to fit with class imbalance observed in the data and γ value is arbitrary 2.0.

Table 6: Summary of metrics used to quantitatively assess the performances of the siUNET and FaultSEG models for geological fault detection task.

METRIC	ADVANTAGES	EQUATION	FAIR VALUE
Precision-Recall AUC (PR-AUC)	• Measure overall performance of the model but does not take into account the quality of localisation • Effective for unbalanced datasets as it does not take into account true negatives • May be misleading if there are many false positives.	$$PRAUC = \int_0^1 Precision(r)dRecall(r)$$	≥ 0.50
Weighted Focal IoU (Intersection over Union)	• Variant of the widely used IoU • Takes into account the quality of the localisation • Adjusts class imbalance by applying weights and giving more weight to smaller and more complex objects. • More suitable for assessing pixel-level accuravy for small objects	$$\frac{\sum_{class} w_c \cdot (y_{true,c} \cdot y_{pred,c})}{\sum_{class} w_c \cdot (y_{true,i} + y_{pred,c} - y_{true,c} \cdot y_{pred,c})} \cdot (1-IoU)^\gamma$$ *Where c is the class, w_c the weight of the class c and γ the focal parameter. In our study, γ=2.0 and w_c are consistent with class imbalance in the data*	≥ 0.50

During training, the performance of the models is estimated in a quantitative manner with metric functions which must consider the class imbalance in the datasets (Table 6): Precision-Recall Area under Curve (PR-AUC), and Weighted Focal Intersection over Union (wF-IoU). These metrics, by measuring the ability of the models to detect faults with a precise location, are essential to optimize the hyperparameters of the model and find the best model for a constant architecture. However, the performances of the different architecture of model (siUNET and FaultSEG) are also estimated in a qualitative manner, through the visual inspections of the predictions, especially in areas that the model has never seen during training.
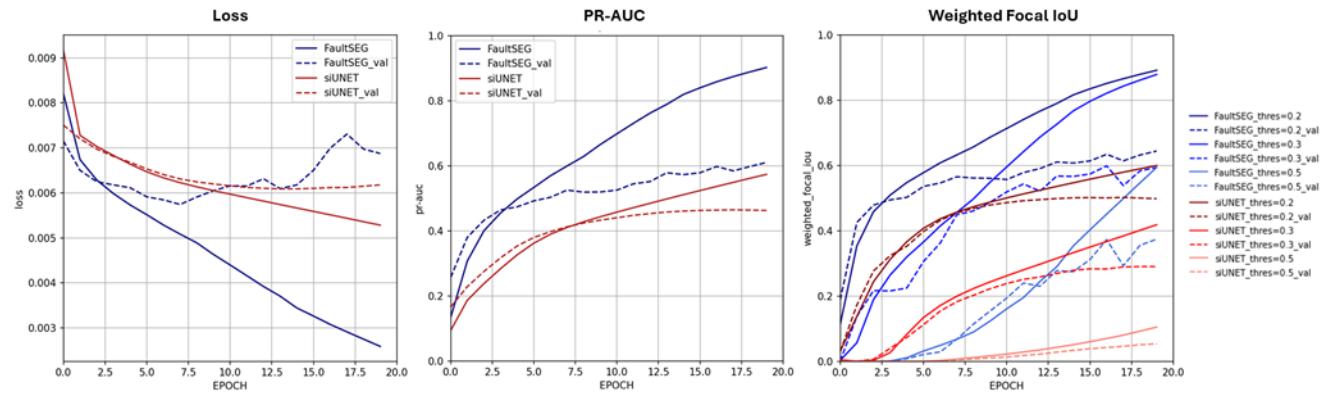
6. RESULTS

Figure 7: Metrics measuring the performance of the siUNET and FaultSEG models for the fault detection. Weighted Focal IoU are calculated for different values of the threshold defining a prediction as true or false. PR-AUC is a global metric that summarises the performance for object detection.

The siUNET and FaultSEG models were both trained on the same augmented dataset with the same hyperparameters (Adam optimizer, 20 epochs and a learning rate of 10^{-5}) and performance results, including loss and metrics, are shown on Figure 7. Note that the Weighted Focal IoU is affected by the threshold that defines a prediction as true or false. Therefore, we calculated this metric for different values of threshold. For the PR-AUC and the wF-IoU, FaultSEG outperforms the siUNET model for the training, validation and test datasets. The values of PR-AUC after 20 epochs, which measured the global performance of the model, are 0.902, 0.610 and 0.595 for training, validation and test respectively for FaultSEG while they are 0.574, 0.463 and 0.449 respectively for siUNET. Therefore, based on PR-AUC, FaultSEG has a fair detection ($\geq$ 0.50), even for validation and test, making it a good candidate for generalization, which is not the case for siUNET. For Weighted Focal IoU, a threshold $\leq$ 0.3 should be considered as good performance for FaultSEG ($\geq$ 0.879, $\geq$ 0.594 and $\geq$ 0.580 for training, validation and test respectively) and $\leq$ 0.2 for siUNET (0.600, 0.498 and 0.453 for training, validation and test respectively). This highlights a better ability of FaultSEG to correctly localize the predicted faults compared to siUNET.

However, the loss and metrics show a clear deviation between the values for training and the validation datasets after 7 epochs, indicating likely overfitting to the training data. This overfitting is also present but to a lesser extent for siUNET after 12 epochs. Note that the FaultSEG after 7 epochs outperforms siUNET avec 12 epochs and reach the fair detection value for both metrics. This probable overfitting raises the question of the generalization of the models from a quantitative point of view.
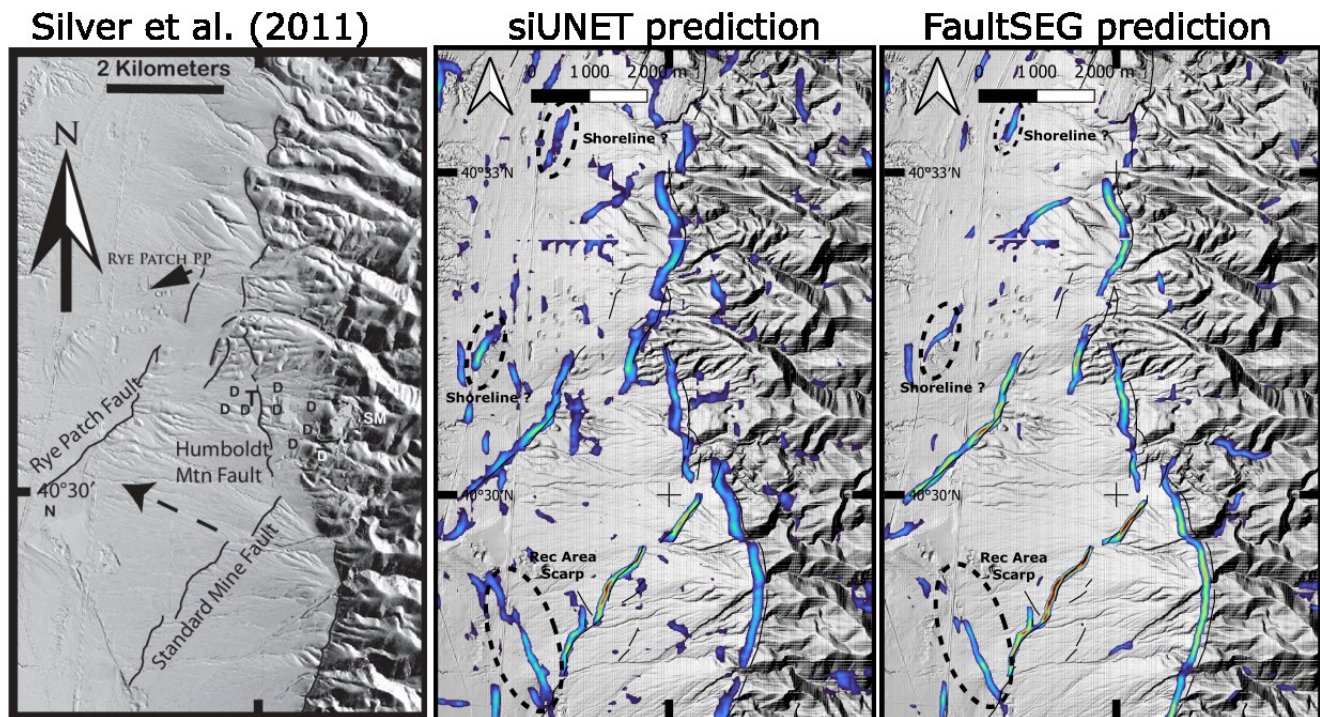

Figure 8: LiDAR image of the western Humboldt Range with faults labelled according to Silver et al. (2011); and siUNET and FaultSEG Quaternary fault prediction in the same area. The detection is qualitatively very good, with fewer artefacts with FaultSEG, but also shows that both siUNET and FaultSEG models detect non faulted objects described by Silver et al. (2011), such as the paleo-shoreline or the Rec Area scarp.

Therefore, we performed predictions with siUNET and FaultSEG on the whole study area (Figure 1) to qualitatively evaluate their prediction performance, and especially the possibility of generalization of both models in the western part of the area (Figure 1). Large-scale results cannot be presented legibly in this publication. However, they show very good detection quality, even in the area dedicated to prediction, so never seen during training, and some example areas are shown in Figure 8 and Figure 9. Although the metrics are below the minimum required for fair detection, siUNET produces interesting qualitative results. However, it shows many small detection artefacts, that are likely to influence the metric values. The qualitative performance of FaultSEG is consistent with the good metric values and confirms that its predictions are better than those of siUNET.

In the Rye Patch area, where a LIDAR fault mapping is available (Silver et al., 2011), the two models siUNET and FaultSEG detect most of the Quaternary faults mapped in the publication, at least as accurately as the previous USGS mapping. Both models are therefore qualitatively very good. Note that the faults to the east of the Rye Patch power plant (Figure 8) are slightly detected by FaultSEG but not by siUNET, confirming the local and qualitative superiority of FaultSEG over. In addition, the siUNET prediction shows more artefact predictions than FaultSEG, which could be pure artefacts or the detection of other surface objects such as the paleo-shoreline, beach ridge (Silver et al., 2011) or canyon.

Another example area around the Leach Hot Springs (Figure 9) confirms the good quality of the detection, as most of the USGS Quaternary faults are detected. Note that the fault trace is derived from the detection image by a proprietary algorithm. It is sometimes even more

accurate than the USGS mapping as some discrepancies > 150 m are observed with a clear offset between the USGS fault line and the topographic break visible on the slope data (Figure 9, area B). New faults are also detected (Figure 9, area A), mainly by FaultSEG and later confirmed by experts looking at the LIDAR data. This shows that the Quaternary fault detection with siUNET and FaultSEG can outperform the USGS mapping. However, as in the western Humboldt Range (Figure 8), the Leach Hot Springs area highlights the ability of FaultSEG, but especially siUNET to detect other object than Quaternary faults. In this case, the detection of a canyon boundary (Figure 9, area B) and stream boundary (Figure 9, area A) raises questions as they are aligned with USGS Quaternary faults.
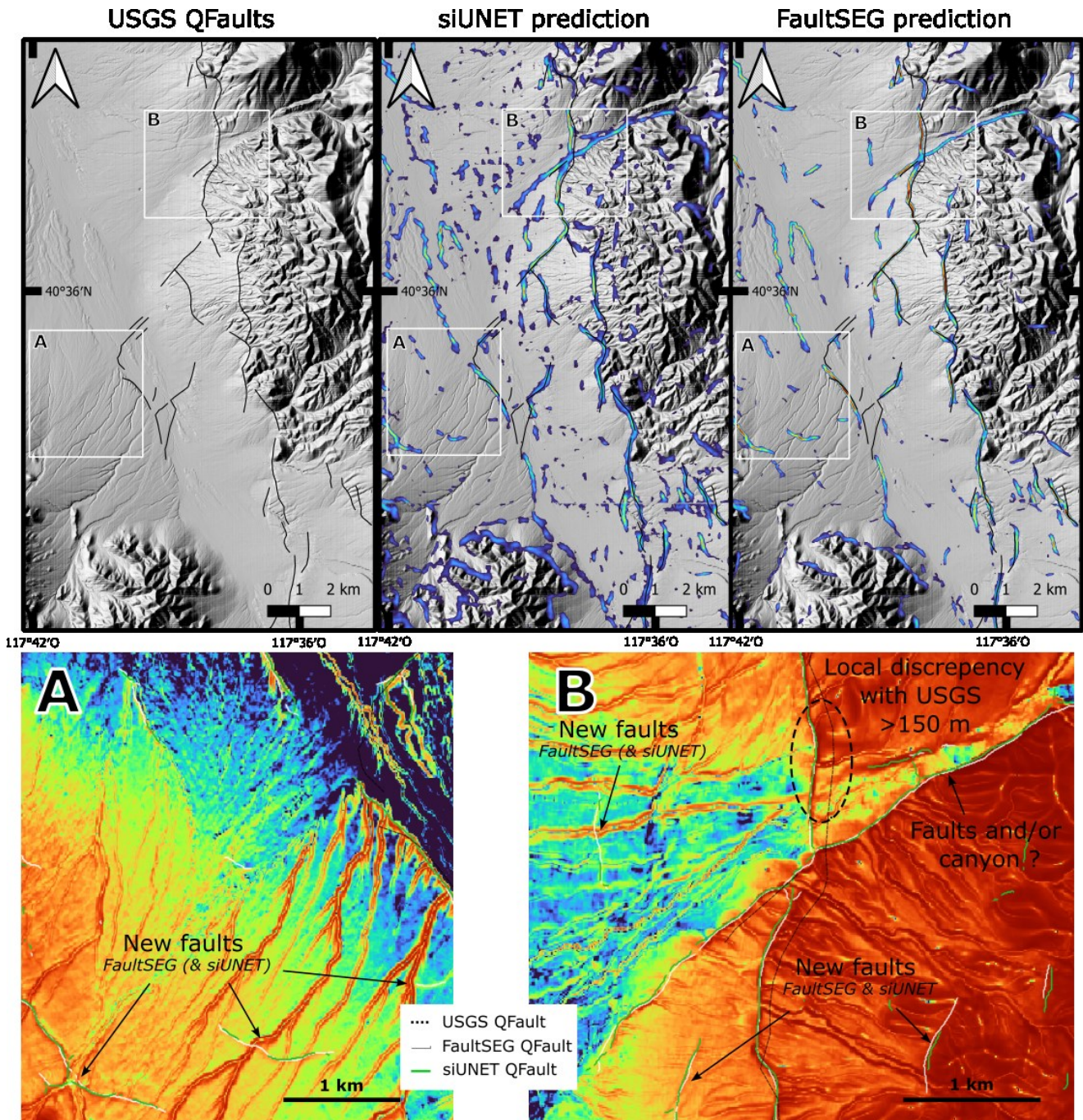

Figure 9: USGS Quaternary fault mapping and siUNET and FaultSEG Quaternary fault detection on the Leach Hot Springs area with zoom on two specific areas: (A) new faults are detected, more accurately by FaultSEG, and confirmed by an expert on LIDAR data; (B) increase in accuracy compared to USGS mapping and possible false detection of a canyon boundary. FaultSEG and siUNET fault traces are extracted from the detection image using a dedicated algorithm.

9

7.   DISCUSSION

The quantitative and qualitative analysis of the predictive performance of siUNET and FaultSEG highlights the difficulties in choosing the right metrics to estimate the performance for such an object detection task: (1) a very high imbalance in the dataset, (2) the complexity of the fault signature on the data used and its similarity to other geomorphological objects, and (3) the fault labels used for training are inherently uncertain as manual fault maps are never exhaustive. With the chosen metrics, only FaultSEG is considered good, while the qualitative analysis shows satisfactory or even good results, even for siUNET.

The high imbalance in the data can be managed manually in the training process and in the metrics by using weights and focusing parameters. However, this adds hyperparameters that require an optimisation phase, as they cannot be determined solely from data statistics, or the nature of the object being searched for. The complex signature of faults is probably the most important issue affecting training and analysis of predictive performance. What is required to confirm the presence of a fault? In the field, without trenches, we generally see clear topographic breaks where it is impossible to measure microstructures that confirm a fault, or microstructural measurements in areas where the LIDAR data do not necessarily indicate a fault. Sites where both are observed at the same time do exist but are actually quite rare compared to the density of faults in the western US. This highlights the need to inform the model that any part of the study area may contain some faults, even if they are not present in the fault label. This could be done by including an adversarial loss term (Goodfellow et al., 2015) or by introducing noise in the true label (Mnih and Hinton, 2012), which will be the subject of further work.

Furthermore, this complexity of fault signature implies that siUNET and FaultSEG, like the fault label mapping expert, may be biased by other objects with similar morphological signatures (paleo-shoreline, canyon, stream). At present, no particular attention has been given to helping the models to distinguish faults from other geomorphological objects. It has been decided to take the risk of predicting too many faults, even if this means deleting them manually afterwards with an expert analysis, rather than missing or incorrectly mapping certain faults. A dedicated learning design with, for example, a paleo-shoreline class and associated labels, could be considered. However, we know that in some cases, faults can be co-located with a paleo-shoreline (geological survey, TLS Geothermics) or with a canyon boundary (Figure 9, area B). An approach to differentiate between them may therefore miss some of these co-located structures. We believe that iterative learning (transfer learning or not), using faults predicted by the model and validated by an expert as fault label, can improve the qualitative and quantitative detection performance as well as discrimination between faults and other geomorphological objects. The more fault examples the model sees, the more likely it is to recognise the signature of a fault in the data. This iterative approach should also be useful in mapping the Quaternary faults outside of central Nevada so in different geological and tectonic contexts such as the Walker Lane (strike-slip motion) and the Rio Grande (narrow rift). This work is ongoing, along with optimization of the hyperparameters to improve learning and hence prediction accuracy.

8.   CONCLUSION

The improvement of fault mapping in Western USA is a key for assessing the geothermal favorability at regional scale, locate the best areas for exploration and build more robust and precise structural models at prospect scale. To complete, precise and homogenize the existing USGS Quaternary Faults database, TLS Geothermics has developed deep learning models, siUNET and FaultSEG, using Convolutionnal Neural Networks to automatically detect faults on remote sensing and satellite data.

After training on a study area in central northern Nevada using fault labels manually mapped by an expert, the two models, but especially FaultSEG, show good qualitative prediction compared to existing Quaternary fault mapping. Quantitatively, the metrics measuring the performance of the models are good for FaultSEG, achieving a fair detection threshold and outperforming the siUNET model. However, some overfitting to the training data is observed for both models, while the prediction over a large test area is qualitatively good. This, together with the tendency of the models to detect morphological objects close to the faults (coastline, canyon, stream), indicates the need to optimize the learning strategy or to significantly increase the number of training data to cover a greater variability of possible fault signatures.

The results of fault mapping using deep learning presented in this study are very encouraging. In the study area, the mapping obtained is at least as complete as existing mapping and often more accurate. Although the current predictions are good, the siUNET and FaultSEG models developed by TLS Geothermics are being optimized to determine the most favorable hyperparameters, which will improve performance and predictions. The proposed iterative learning strategy is also being implemented and should rapidly lead to improved predictions and better generalization of the models. We are in the process of producing a new map of Quaternary faults across the western USA, where LIDAR data allow, which will aid exploration of fault-controlled geothermal systems and understanding of tectonic processes.

9.   REFERENCES

Atwater, T., Stock, J., 1998. Pacific-North America Plate Tectonics of the Neogene Southwestern United States: An Update. Int. Geol. Rev. 40, 375–402. https://doi.org/10.1080/00206819809465216

Baghbanan, A., Jing, L., 2008. Stress effects on permeability in a fractured rock mass with correlated fracture length and aperture. Int. J. Rock Mech. Min. Sci. 45, 1320–1334.

Barton, C.A., Hickman, S., Morin, R.H., Zoback, M.D., Finkbeiner, T., Sass, J., Benoit, D., 1997. Fracture Permeability and its Relationship to In-Situ Stress in the Dixie Valley, Nevada, Geothermal Reservoir. Proc. Twenty-Second Workshop Geotherm. Reserv. Engineenng Stanf. Unlverslty Stanf. Calif.

Barton, C.A., Zoback, M.D., Moos, D., 1995. Fluid flow along potentially active faults in crystalline rock. Geology 23, 683–686.

Bense, V.F., Gleeson, T., Loveless, S.E., Bour, O., Scibek, J., 2013. Fault zone hydrogeology. Earth-Sci. Rev. 127, 171–192.

Boureau, Y.-L., Ponce, J., LeCun, Y., 2010. A Theoretical Analysis of Feature Pooling in Visual Recognition. Proc. 27th Int. Conf. Mach. Learn. ICML-10.

Buslaev, A., Iglovikov, V.I., Khvedchenya, E., Parinov, A., Druzhinin, M., Kalinin, A.A., 2020. Albumentations: Fast and Flexible Image Augmentations. Information 11, 125. https://doi.org/10.3390/info11020125

Caine, J.S., Evans, J.P., Forster, C.B., 1996. Fault zone architecture and permeability structure. Geology 24, 1025–1028.

Chester, F.M., Logan, J.M., 1986. Implications for mechanical properties of brittle faults from observations of the Punchbowl fault zone, California. Pure Appl. Geophys. 124, 79–106. https://doi.org/10.1007/BF00875720

Curewitz, D., Karson, J.A., 1997. Structural settings of hydrothermal outflow: Fracture permeability maintained by fault propagation and interaction. J. Volcanol. Geotherm. Res. 79, 149–168. https://doi.org/10.1016/S0377-0273(97)00027-9

Das, V., Pollack, A., Wollner, U., Mukerji, T., 2019. Convolutional neural network for seismic impedance inversion. GEOPHYSICS 84, R869–R880. https://doi.org/10.1190/geo2018-0838.1

Detwiler, R.L., Morris, J.P., 2018. Fracture Initiation, Propagation, and Permeability Evolution, in: Vialle, S., Ajo-Franklin, J., Carey, J.W. (Eds.), Geophysical Monograph Series. Wiley, pp. 119–135. https://doi.org/10.1002/9781119118657.ch5

Ding, J., Chen, B., Liu, H., Huang, M., 2016. Convolutional Neural Network With Data Augmentation for SAR Target Recognition. IEEE Geosci. Remote Sens. Lett. 1–5. https://doi.org/10.1109/LGRS.2015.2513754

Evans, J.P., Forster, C.B., Goddard, J.V., 1997. Permeability of fault-related rocks, and implications for hydraulic structure of fault zones. J. Struct. Geol. 19, 1393–1404.

Faulds, J., Coolbaugh, M., Bouchot, V., Moek, I., Oguz, K., 2010. Characterizing structural controls of geothermal reservoirs in the Great Basin, USA, and Western Turkey: developing successful exploration strategies in extended terranes, in: World Geothermal Congress 2010. pp. 11-p.

Faulds, J., Hinz, N., 2015. Favorable tectonic and structural settings of geothermal systems in the Great Basin region, western USA: Proxies for discovering blind geothermal systems, in: Proceedings World Geothermal Congress, Melbourne, Australia, 19-25 April 2015. Nevada Bureau of Mines and Geology, University of Nevada, Reno.

Faulds, J.E., Henry, C.D., Hinz, N.H., 2005. Kinematics of the northern Walker Lane: An incipient transform fault along the Pacific–North American plate boundary. Geology 33, 505–508.

Faulkner, D.R., Mitchell, T.M., Jensen, E., Cembrano, J., 2011. Scaling of fault damage zones with displacement and the implications for fault growth processes. J. Geophys. Res. 116, B05403. https://doi.org/10.1029/2010JB007788

Gale, J. E., 1982. Assessing the permeability characteristics of fractured rock.

Gale, John E., 1982. The effects of fracture type (induced versus natural) on the stress-fracture closure-fracture permeability relationships, in: ARMA US Rock Mechanics/Geomechanics Symposium. ARMA, p. ARMA-82.

Gao, B., Pan, D.D., Xu, Z.H., Zhang, L.W., Zhao, S.L., 2020. Effect of Density, Trace Length, Aperture, and Direction Angle on Permeability Performance of Fracture Networks. Int. J. Geomech. 20, 04020116. https://doi.org/10.1061/(ASCE)GM.1943-5622.0001718

Goodfellow, I.J., Shlens, J., Szegedy, C., 2015. Explaining and Harnessing Adversarial Examples. https://doi.org/10.48550/arXiv.1412.6572

Hammond, W.C., Thatcher, W., 2007. Crustal deformation across the Sierra Nevada, northern Walker Lane, Basin and Range transition, western United States measured with GPS, 2000–2004. J. Geophys. Res. Solid Earth 112.

Hornik, K., Stinchcombe, M., White, H., 1989. Multilayer feedforward networks are universal approximators. Neural Netw. 2, 359–366. https://doi.org/10.1016/0893-6080(89)90020-8

Johnson, K., Nissen, E., Saripalli, S., Arrowsmith, J.R., McGarey, P., Scharer, K., Williams, P., Blisniuk, K., 2014. Rapid mapping of ultrafine fault zone topography with structure from motion. Geosphere 10, 969–986. https://doi.org/10.1130/GES01017.1

Jolie, E., Moeck, I., Faulds, J.E., 2015. Quantitative structural–geological exploration of fault-controlled geothermal systems—a case study from the Basin-and-Range Province, Nevada (USA). Geothermics 54, 54–67.

Jones, C.H., Wernicke, B.P., Farmer, G.L., Walker, J.D., Coleman, D.S., McKenna, L.W., Perry, F.V., 1992. Variations across and along a major continental rift: An interdisciplinary study of the Basin and Range Province, western USA. Tectonophysics 213, 57–96.

Kaven, J.O., Hickman, S.H., Davatzes, N.C., 2011. Micro-seismicity, fault structure and hydraulic compartmentalization within the Coso Geothermal Field, California, in: Proceedings, Thirty-Sixth Workshop on Geothermal Resrvoir Engineering.

Kreemer, C., Blewitt, G., Hammond, W.C., Oldow, J., Cashman, P., 2009. Geodetic constraints on contemporary deformation in the northern Walker Lane: 2. Velocity and strain rate tensor analysis. Late Cenozoic Struct. Evol. Gt. Basin–Sierra Nev. Transit. Geol. Soc. Am. Spec. Pap. 447, 17–31.

Krizhevsky, A., Sutskever, I., Hinton, G.E., 2012. ImageNet Classification with Deep Convolutional Neural Networks, in: Advances in Neural Information Processing Systems. Curran Associates, Inc.

LeCun, Y., Bengio, Y., Hinton, G., 2015. Deep learning. nature 521, 436–444.

LeCun, Y., Bengio, Y., Laboratories, T.B., 1995. Convolutional Networks for Images, Speech, and Time-Series. Handb. Brain Theory Neural Netw. 336110.

LeCun, Y., Boser, B., Denker, J., Henderson, D., Howard, R., Hubbard, W., Jackel, L., 1989. Handwritten Digit Recognition with a Back-Propagation Network, in: Advances in Neural Information Processing Systems. Morgan-Kaufmann.

Lin, T.-Y., Goyal, P., Girshick, R., He, K., Dollár, P., 2018. Focal Loss for Dense Object Detection. https://doi.org/10.48550/arXiv.1708.02002

MacKnight, R.B., Silver, E., Kennedy-Bowdoin, T., Pickles, W.L., Waibel, A., 2004. Remote sensing analysis of structure and geothermal potential of the Humboldt Block, Nevada, in: IGARSS 2004. 2004 IEEE International Geoscience and Remote Sensing

Symposium. Presented at the IGARSS 2004. 2004 IEEE International Geoscience and Remote Sensing Symposium, p. 629. https://doi.org/10.1109/IGARSS.2004.1369106

Mattéo, L., Manighetti, I., Tarabalka, Y., Gaucel, J., Van Den Ende, M., Mercier, A., Tasar, O., Girard, N., Leclerc, F., Giampetro, T., Dominguez, S., Malavieille, J., 2021. Automatic Fault Mapping in Remote Optical Images and Topographic Data With Deep Learning. J. Geophys. Res. Solid Earth 126, e2020JB021269. https://doi.org/10.1029/2020JB021269

Mitchell, T.M., Faulkner, D.R., 2009. The nature and origin of off-fault damage surrounding strike-slip fault zones with a wide range of displacements: A field study from the Atacama fault system, northern Chile. J. Struct. Geol. 31, 802–816.

Mnih, V., Hinton, G., 2012. Learning to Label Aerial Images from Noisy Data. Proc. 29th Int. Conf. Mach. Learn. ICML-12.

Nair, V., Hinton, G.E., 2010. Rectified Linear Units Improve Restricted Boltzmann Machines. Proc. 27th Int. Conf. Mach. Learn. ICML-10.

Palafox, L.F., Hamilton, C.W., Scheidt, S.P., Alvarez, A.M., 2017. Automated detection of geological landforms on Mars using Convolutional Neural Networks. Comput. Geosci. 101, 48–56.

Ronneberger, O., Fischer, P., Brox, T., 2015. U-Net: Convolutional Networks for Biomedical Image Segmentation, in: Navab, N., Hornegger, J., Wells, W.M., Frangi, A.F. (Eds.), Medical Image Computing and Computer-Assisted Intervention – MICCAI 2015, Lecture Notes in Computer Science. Springer International Publishing, Cham, pp. 234–241. https://doi.org/10.1007/978-3-319-24574-4_28

Russakovsky, O., Deng, J., Su, H., Krause, J., Satheesh, S., Ma, S., Huang, Z., Karpathy, A., Khosla, A., Bernstein, M., Berg, A.C., Fei-Fei, L., 2015. ImageNet Large Scale Visual Recognition Challenge. Int. J. Comput. Vis. 115, 211–252. https://doi.org/10.1007/s11263-015-0816-y

Siler, D.L., 2023. Structural discontinuities and their control on hydrothermal systems in the Great Basin, USA. Geoenergy 1, geoenergy2023. https://doi.org/10.1144/geoenergy2023-009

Siler, D.L., Faulds, J.E., Mayhew, B., McNamara, D.D., 2016. Analysis of the favorability for geothermal fluid flow in 3D: Astor Pass geothermal prospect, Great Basin, northwestern Nevada, USA. Geothermics 60, 1–12.

Siler, D.L., Hinz, N.H., Faulds, J.E., 2018. Stress concentrations at structural discontinuities in active fault zones in the western United States: Implications for permeability and fluid flow in geothermal fields. Bulletin 130, 1273–1288.

Silver, E., MacKnight, R., Male, E., Pickles, W., Cocks, P., Waibel, A., 2011. LiDAR and hyperspectral analysis of mineral alteration and faulting on the west side of the Humboldt Range, Nevada. Geosphere 7, 1357–1368. https://doi.org/10.1130/GES00673.1

Simonyan, K., Zisserman, A., 2015. Very Deep Convolutional Networks for Large-Scale Image Recognition. https://doi.org/10.48550/arXiv.1409.1556

Sturman, O., Von Ziegler, L., Schläppi, C., Akyol, F., Privitera, M., Slominski, D., Grimm, C., Thieren, L., Zerbi, V., Grewe, B., Bohacek, J., 2020. Deep learning-based behavioral analysis reaches human accuracy and is capable of outperforming commercial solutions. Neuropsychopharmacology 45, 1942–1952. https://doi.org/10.1038/s41386-020-0776-y

U.S. Geological Survey and Nevada Bureau of Mines and Geology, Quaternary fault and fold database for the United States, accessed, at: https://www.usgs.gov/natural-hazards/earthquake-hazards/faults.

U.S. Geological Survey, 2019, USGS 3D Elevation Program Digital Elevation Model, accessed at URL https://elevation.nationalmap.gov/arcgis/rest/services/3DEPElevation/ImageServer.

Vouldodimos, A., Doulamis, N., Doulamis, A., Protopapadakis, E., 2018. Deep Learning for Computer Vision: A Brief Review. Comput. Intell. Neurosci. 2018, 1–13. https://doi.org/10.1155/2018/7068349

Waldeland, A.U., Jensen, A.C., Gelius, L.-J., Solberg, A.H.S., 2018. Convolutional neural networks for automated seismic interpretation. Lead. Edge 37, 529–537. https://doi.org/10.1190/tle37070529.1

Wesnousky, S.G., 1988. Seismological and structural evolution of strike-slip faults. Nature 335, 340–343.

Wrona, T., Pan, I., Bell, R.E., Gawthorpe, R.L., Fossen, H., Brune, S., 2021. 3D seismic interpretation with deep learning: A brief introduction. Lead. Edge 40, 524–532. https://doi.org/10.1190/tle40070524.1

Xiong, W., Ji, X., Ma, Y., Wang, Y., AlBinHassan, N.M., Ali, M.N., Luo, Y., 2018. Seismic fault detection with convolutional neural network. GEOPHYSICS 83, O97–O103. https://doi.org/10.1190/geo2017-0666.1